Journal of Nuclear Materials 487 (2017) 433–442

Contents lists available at ScienceDirect

Journal of Nuclear Materials

journal homepage: www.elsevier.com/locate/jnucmat

Microstructural comparison of effects of hafnium and titanium additions in spark-plasma-sintered Fe-based oxide-dispersion strengthened alloys

Yina Huang [a, f, *], Hongtao Zhang [b], Maria A. Auger [a], Zuliang Hong [a], Huanpo Ning [d, e], Michael J. Gorley [a, c], Patrick S. Grant [a], Michael J. Reece [d, e], Haixue Yan [d, e], Steve G. Roberts [a, c]

[a] Department of Materials, University of Oxford, Oxford OX1 3PH, UK
[b] Department of Materials, Loughborough University, Leicestershire, LE11 3TU, UK
[c] CCFE, Culham Science Centre, Abingdon, Oxon, OX14 3DB, UK
[d] School of Engineering of Materials Science, Queen Mary University of London, London, E1 4NS, UK
[e] Nanoforce Technology Ltd, London, E1 4NS, UK
[f] School of Electronic Science & Applied Physics, Hefei University of Technology, Hefei, Anhui 230009, China

ARTICLE INFO

Article history:
Received 11 October 2016
Received in revised form
25 January 2017
Accepted 20 February 2017
Available online 21 February 2017

ABSTRACT

Two oxide dispersion strengthened alloys: 14Cr-0.25Y_2O_3-0.22Hf (wt.%) and Fe-14Cr-0.25Y_2O_3-0.4Ti (wt.%) were fabricated by mechanical alloying and subsequently consolidated by spark plasma sintering (SPS). Electron backscatter diffraction showed grain sizes in the range 0.5–15 μm in both alloys. Transmission electron microscopy and scanning transmission electron microscopy showed a homogeneous distribution of nano-oxides precipitated during SPS. Using high resolution transmission electron microscopy, energy dispersive X-ray spectroscopy and atom probe tomography, several different oxide phases were found in both alloys, but the majority of dispersoids were Y-Hf-O type in Fe-14Cr-0.25Y_2O_3-0.22Hf and Y-Ti-O type in Fe-14Cr-0.25Y_2O_3-0.4Ti. There were a variety of orientation relationships between the different dispersoids and the ferritic matrix. Both alloys had dispersoid densities of ~$10^{23}/m^3$, with average diameters of 4.3 nm and 3.5 nm in the 0.22Hf and 0.4Ti containing alloys, respectively. Per atom added, Hf (0.07 at.%) is suggested to be more potent than Ti (0.46 at.%) in refining the nano-oxides.

1. Introduction

Oxide dispersion strengthened (ODS) alloys have been studied intensively for a wide variety of applications [1–5] because of their excellent high temperature strength and improved creep resistance. In a radiation environment in which materials are exposed to an ion or neutron flux, the high density of oxide dispersoids are able to trap or act as a sink for vacancies, interstitials and gas atoms, improving resistance to radiation damage and to gas accumulation [6].

ODS alloys are typically fabricated by mechanical alloying of an alloy powder and a minor fraction of oxide powder, followed by consolidation through hot extrusion or hot isostatic pressing (HIP) of degassed cans [1,7–10]. Recently, spark plasma sintering (SPS), also known as the field assisted sintering technique (FAST), has been introduced as an alternative for the consolidation of powders, including ODS-based powders [11–14]. The principal advantages of SPS/FAST are to reduce the thermal exposure of powders (e.g. typically 1000–1200 °C for 4 h in HIP), to reduce processing times and costs, and potentially to better retain metastable microstructural features such as fine grains of one micron or smaller.

In Fe-based ODS alloys proposed for structural applications in the nuclear fission or fusion power plant environment, titanium additions, typically to a Fe-14Cr (wt.%) ferritic type base alloy, have been shown to produce a refining effect on the resulting dispersoids, and a change from Y-O to Y-Ti-O containing oxides [15–19], although the precise mechanism for refinement has not yet been clarified e.g. the balance between promotion of nucleation or

* Corresponding author. School of Electronic Science & Applied Physics, Hefei University of Technology, Hefei, Anhui 230009, China.
E-mail address: huangyina1981@hotmail.com (Y. Huang).

http://dx.doi.org/10.1016/j.jnucmat.2017.02.030

growth restriction. Nonetheless, these studies suggest the possibility that other elements may show a similar refining effect, and by understanding the potency (or not) of other elements, greater understanding on the role of Ti may be obtained, or more powerful refiners discovered.

In this paper, we build on the relatively few papers on the effect of hafnium addition to ODS alloys [20–23], for example the suggested refining effect of hafnium on oxides in austenitic ODS stainless steels [20], by using rapid consolidation by SPS/FAST of ferritic powders followed by the application of a range of high-resolution characterization techniques, including transmission electron microscopy (TEM), scanning transmission electron microscopy (STEM), energy dispersive spectroscopy (EDS), and atom probe tomography (APT). To elucidate the effect of Hf, we study "back-to-back" Fe-14Cr-0.25Y_2O_3-0.22Hf (wt.%, "14 YH") and Fe-14Cr-0.25Y_2O_3-0.4Ti ("14 YT"), and the characterization focuses on a comparison of the resulting dispersoid types. Both alloys contained a high dispersoid number density of $10^{23}/m^3$. In 14 YH, most dispersoids were composed of Y-Hf-O type with an average size of 4.3 nm while in 14 YT, most dispersoids were composed of Y-Ti-O type with an average size of 3.5 nm.

2. Experimental

2.1. ODS alloy processing

Argon gas atomized Fe-14Cr wt.% pre-alloyed powders (<150 μm in diameter, Aubert & Duval, France), elemental Hf and Ti powder (−325 mesh, 99.5%, Alfa Aesar, UK) and Y_2O_3 powder with a particle size ranging from 20 to 40 nm (Pi-Kem Ltd, UK) were used as starting materials for the mechanically alloyed powders with nominal composition Fe-14Cr-0.25Y_2O_3-0.22Hf (wt.%, "14 YH") and Fe-14Cr-0.25Y_2O_3-0.4Ti (wt%, "14 YT"). The atomic percentage of Hf in 14 YH and Ti in 14 YT was 0.07 and 0.46 at.%, respectively. Milling was performed in 99.999% purity Ar using a planetary ball mill (Pulverisette 6, Fritsch GmbH, Germany) with a chrome-steel bowl (500 ml), AISI 52100 steel balls with a ball-to-powder weight ratio of 10:1 and a rotational speed of 150 rpm. A steady-state condition/microstructure of the 14 YH and 14 YT powder was achieved after milling for 60 h s [39]. The milled powder was loaded into a graphite mould lined with graphite paper in an Ar-filled glove box for SPS consolidation.

SPS consolidation was performed at FCT Systeme GmbH, Rauenstein, Germany, in a vacuum of 5–8 Pa at 1150 °C for 5min under a peak uniaxial pressure of 50 MPa. The heating rate applied was 100 °C/min. The dimensions of the consolidated 14 YH and 14 YT samples were typically 20 mm in diameter and 5 mm in thickness; further details are available in Ref. [24].

2.2. TEM specimen preparation

Alloys 14 YH and 14 YT were mechanically polished to a 4000 grit finish using SiC paper. Transmission electron microscopy (TEM) specimens were then prepared by focussed ion beam (FIB) lift-out using 30 kV and finally 5 kV Ga^+ ions in a Zeiss Auriga FIB fitted with a scanning electron microscope (SEM). The Pt grids used were made by cutting a standard Pt mesh grid in half so that the grid-ends could be used for hosting lift-out samples (Fig. 1a). After being welded by Pt deposition to the grid, lift-out foils were further thinned by 30 kV Ga^+ ions at 1.5° tilt respect to the sample surface and finally 5 kV Ga^+ ions at 7° tilt respect to the sample surface, reaching a 120–150 nm sample thickness (estimated from the FIB image) with three thicker edges retained as a "frame" to hold the lamella (Fig. 1b).

Near-surface ion-beam damage on FIBed specimens is inevitable and can hamper micro-structural analysis [25–27]. Calculations using SRIM (Stopping and Range of Ions in Matter) suggested a ~20 nm deep damaged layer from the 30 kV Ga ions at 1.5° tilt respect to the sample surface and a ~7 nm deep damaged layer from the 5 kV Ga ions at 7° tilt respect to the sample surface (Fig. 2). Hence, a final flash electro-polishing procedure was used to remove the damaged layer on both sides of the lamellae [28]. The specimen, held in Au coated tweezers, acted as the cathode and a curved stainless steel sheet was used as the anode. The solution was stirred during electro-polishing using a ceramic–coated stirring bar, spun magnetically. The polishing solution was 4% $HClO_4$ + 96% ethanol at −30 °C, with a polishing voltage of 12 V. Polishing times were typically 0.2 s, removing ~20 nm from each side of the foil. After polishing, the foil was rinsed with ethanol at −30 °C and then ethanol at room temperature. Specimens were transferred to TEM examination right after electro-polishing. Fig. 3 shows an example of typical TEM micrographs of Fe-14Cr-0.25Y_2O_3 (wt.%) before and after flash electro-polishing, indicating the importance of the flash electro-polishing approach.

2.3. APT specimen preparation

Samples for APT characterization were prepared by mechanically cutting 0.5 × 0.5 × 15 mm rods from the bulk material. The rod sides were mechanically polished to a 1200 grit finish using SiC paper, followed by electropolishing in two stages at room temperature to produce needle-shaped samples with a tip radius <100 nm [34,35]:

Stage 1: Voltage between 15 and 7 V in a 25 vol% perchloric acid (60%) and 75 vol% acetic acid solution; and.

Stage 2: Voltage between 7 and 4 V in a 2 vol% perchloric acid (60%) and 98 vol% 2-butoxyethanol solution.

2.4. Characterization techniques

Alloy grain structures were investigated by electron backscatter diffraction (EBSD) in a JEOL 6500F operated at 20 kV, a probe current of 10 nA, a probe step size of 50 nm and a mapping area of ~8 × 20 μm^2. More detailed microstructural studies, including investigating the structure and interfaces of dispersoids were carried out by TEM using a JEOL 2100 at 200 kV and a JEOL 3000F at 300 kV. Chemical profiles of the dispersoids and interfaces were examined by STEM-EDS in a JEOL 2100.

Atom probe tomography (APT) analysis was carried out in a CAMECA LEAP 3000HR™ instrument operating in laser-pulsing mode at a repetition rate of 200 kHz, using a laser energy of 0.4 nJ and maintaining a base temperature of 50 K. APT data reconstruction was carried out using CAMECA IVAS™ software. Y, Y-O and Hf-O were selected as core-cluster ions. The maximum separation method was used to identify clusters [36]. A minimum number (N_{min}) of 9 ions in a maximum separation distance (d_{max}) of 1.2 nm were taken as the cluster selection parameters, finding 162 clusters in the analyzed volume. 3D chemical maps with atomic spatial resolution were reconstructed. The cluster size was calculated in terms of the radius (or diameter) of gyration [37]. Best-fit ellipsoids were applied to characterise the shape of the clusters. The smallest, middle and largest characteristic lengths of the best-fit ellipsoids allow estimation of the oblateness (smallest characteristic length/middle characteristic length) and aspect ratio (middle characteristic length/largest characteristic length) of the clusters, defining sphere, rod, lath or disc shapes [38]. Fuller details of the APT characterization of alloy 14 YT are given in Ref. [24].

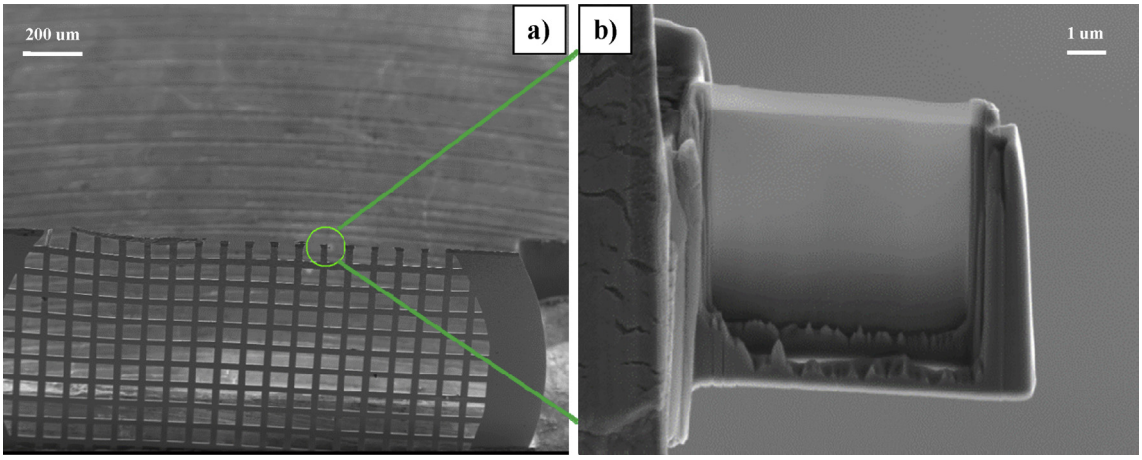

Fig. 1. (a) Low magnification SEM images of a FIB lift out specimen on half cut Pt grid; and (b) SEM image of a lamella ready for TEM inspection.

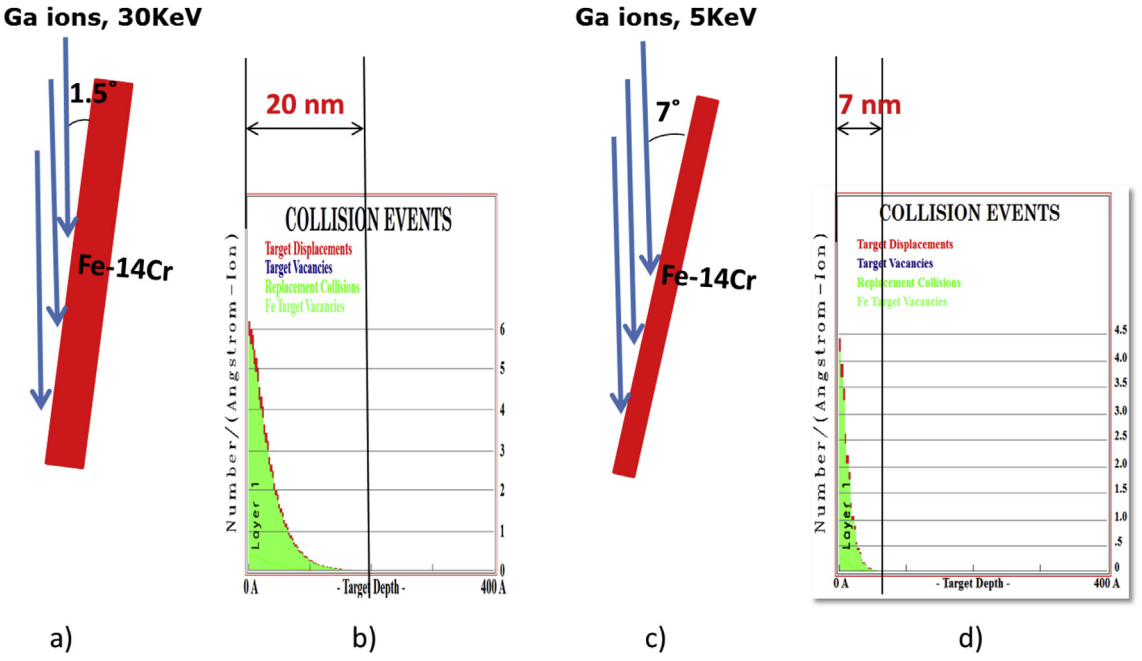

Fig. 2. (a) Schematic of the sample at 1.5° tilt from the 30 kV Ga ion beam in the FIB thinning process; (b) SRIM calculations of FIB damage in Fe-14Cr alloy for the conditions and geometry displayed in (a); (c) schematic of the sample at 7° tilt from the 5 kV Ga ion beam in the final FIB thinning process; and (d) SRIM calculations of FIB damage in Fe-14Cr alloys for the conditions and geometry displayed in (c).

3. Results

3.1. EBSD

Fig. 4(a) and (b) show EBSD grain orientation maps for the 14 YH and 14 YT alloys. All grains were ferritic and grain orientations (surface normal) are colour-coded as in the inset standard triangles. Grain boundaries were defined as having misorientation >5° and sub-grains as having misorientation between 0° and 5°. Both 14 YH and 14 YT had random grain orientations and grain sizes in the range 0.5 μm–15 μm, with some occasional very large grains, as shown in Fig. 4a. Previous studies [29,30] have shown that inhomogeneity of the yttrium distribution associated with inhomogeneous precipitation and pinning of grain boundaries, along with abnormal grain coarsening behavior, can lead to the formation of occasional larger ferrite grains.

3.2. TEM and STEM

The TEM micrographs in Fig. 5 show that the ferrite grains of both alloy types had relatively low dislocation densities, implying that much of the cold work of room temperature high energy ball milling was eliminated, through annealing and recovery during the short time at elevated temperature during SPS. Dispersoids in 14 YH and 14 YT appear to be homogeneously distributed. Also, no porosity was observed in either alloy.

The STEM annular dark field (ADF) micrographs in Fig. 6 show details of typical dispersoids. In 14 YH (Fig. 6 a) the dispersoids were usually as small as 1–5 nm in diameter but with a few larger dispersoids of >30 nm and the dispersoids were mostly spherical with a few of cubic morphology. In 14 YT (Fig. 6 b), dispersoids were more uniform in diameter and were mostly cubic while the larger dispersoids (ranging from 9 nm to 15 nm) were mostly spherical. In

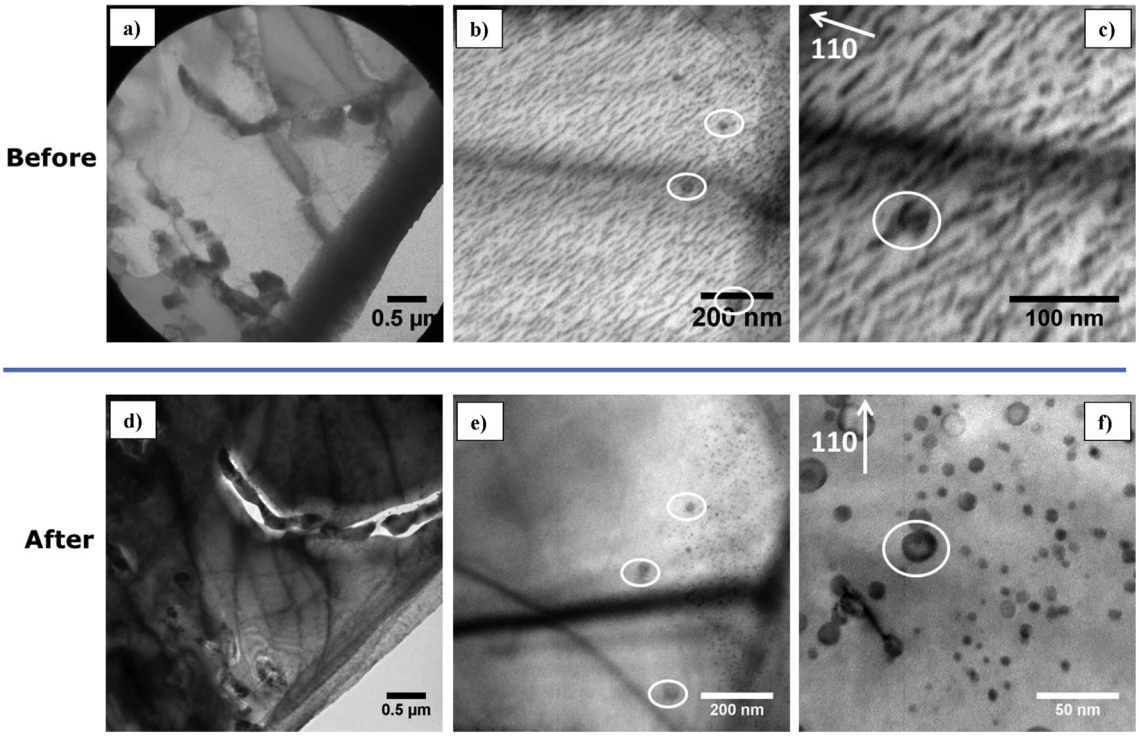

Fig. 3. An example of typical TEM micrographs before and after flash electro-polishing of HIPed Fe-14Cr-0.25Y_2O_3 (wt%). (a,b and c are before flash electro-polishing; d, e and f are after flash electro-polishing). The white circles indicate the same dispersoids before and after flash electro-polishing.

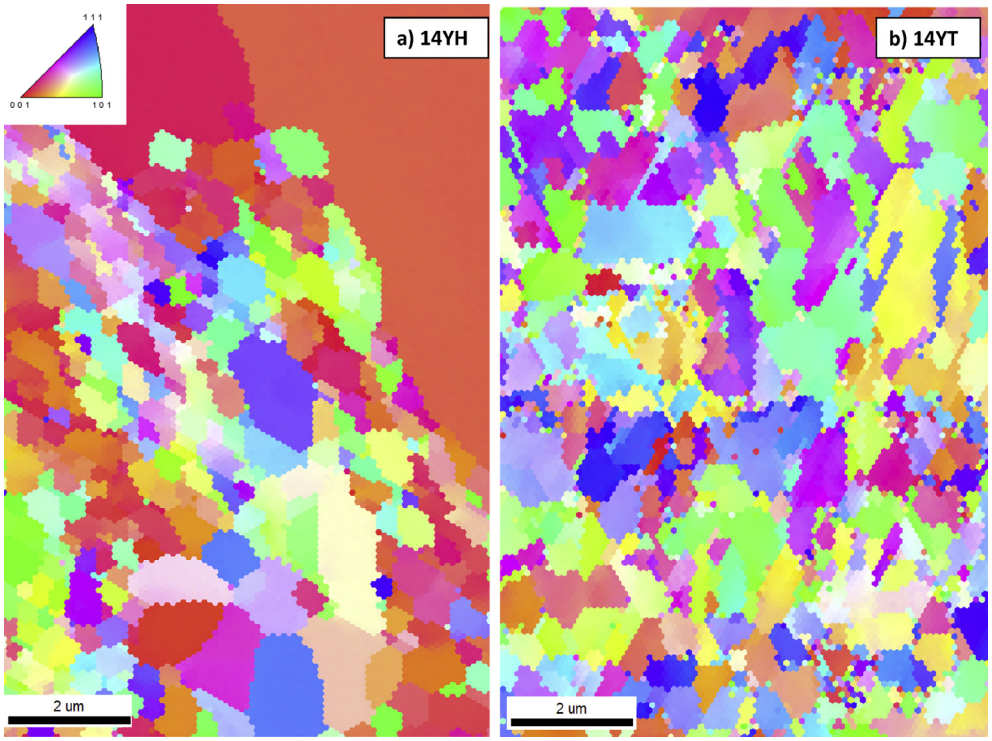

Fig. 4. EBSD maps of alloys (a) 14 YH and (b) 14 YT.

both alloys, some dispersoids (circled in white) showed misfit Moiré fringes confirming that the particles were crystalline and potentially coherent or semi-coherent (partial coherent) with the ferritic matrix [31,32].

The size of ~1300 dispersoids in each material was investigated using Image J image analysis software. The average size of dispersoids was described as a diameter if they were near-spherical, as a diagonal distance if cubic or rectangular, or as the longest internal

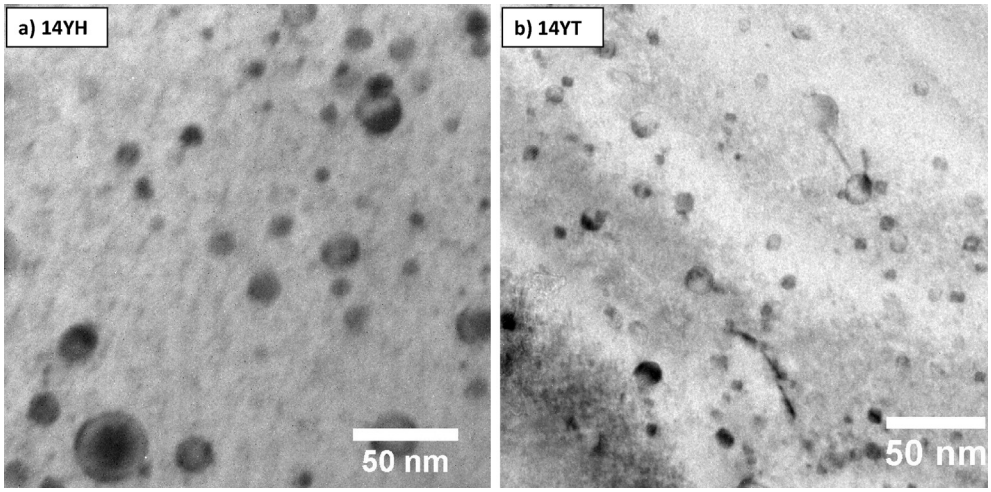

Fig. 5. Bright-field TEM micrographs of (a) 14 YH and (b) 14 YT.

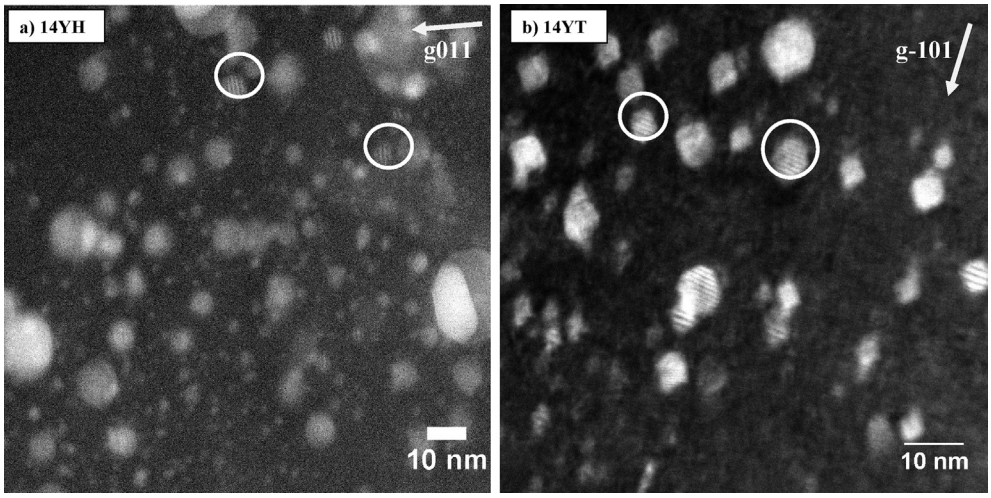

Fig. 6. STEM micrographs of alloys 14 YH and 14 YT (a) STEM ADF micrograph of 14 YH at high magnification; and (b) STEM ADF micrograph of 14 YT at high magnification. In both cases, white circles indicate dispersoids with misfit Moiré fringes.

distance if more irregular in shape. In 14 YH, the average dispersoid size was ~4.3 nm with a density of $0.8 \times 10^{23}/m^3$ while in 14 YT the average dispersoid size was ~3.5 nm with a density of $1.04 \times 10^{23}/m^3$. Fig. 7 compares the size distributions obtained from 14 YH and 14 YT, with dispersoids smaller than 10 nm comprising ~92% in 14 YH and ~95% in 14 YT.

3.3. HR-TEM

Fig. 8(a) shows an HR-TEM micrograph of the matrix of alloy 14YH with a highlighted dispersoid while Fig. 8(b) shows the corresponding FFT image on Z = [111]. Matrix planes are indexed in white while the related planes in the dispersoids are indexed in yellow. The dispersoid inter-planar spacing was 0.249 nm and was coherent with the matrix on {110}.

Fig. 9(a) shows an HR-TEM micrograph of another dispersoid in 14YH and its corresponding FFT image on Z [100] is shown in Fig. 9(b). The inter-planar spacings of the two planes at 75° to each other were 0.515 nm and 0.264 nm, and the dispersoid had one plane coherent with matrix on {200}.

Fig. 10(a) and (b) show an HR-TEM micrograph of alloy 14YT and the corresponding FFT images from Z [100] respectively. In this case, the dispersoid in Fig. 10a had no resolvable orientation with the matrix.

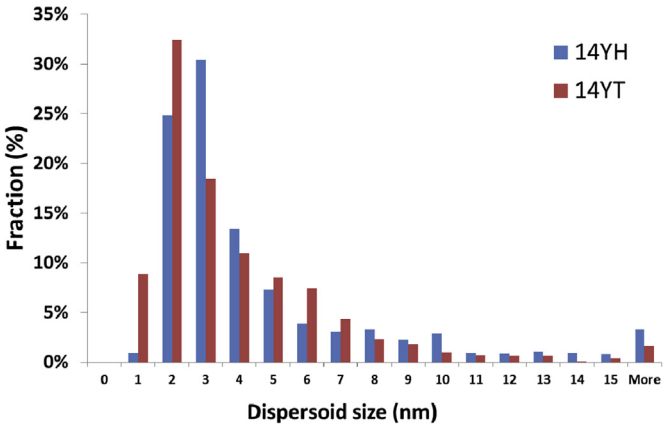

Fig. 7. Dispersoid size (diameter) number distribution in alloys 14 YH and 14 YT.

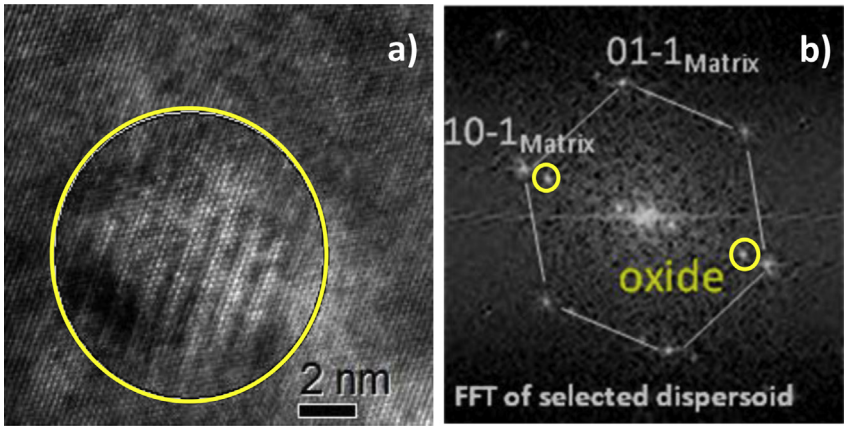

Fig. 8. a) HRTEM micrographs on Z[111] of the ferrite matrix in alloy 14 YH; and (b) corresponding FFT from the particle shown in (a).

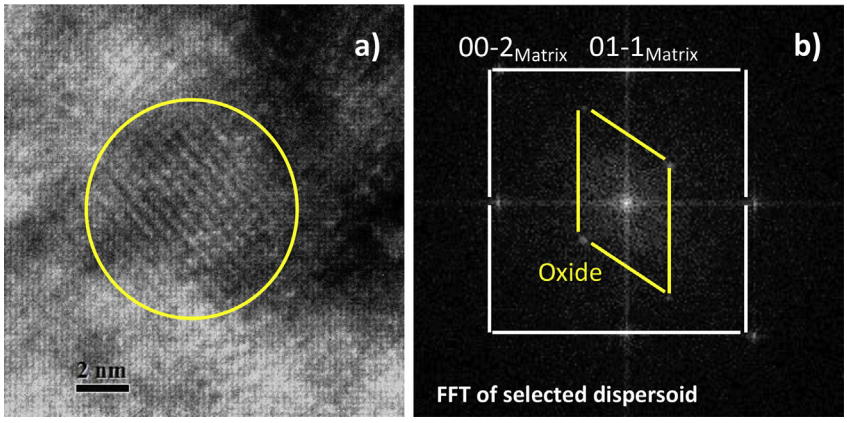

Fig. 9. (a) HRTEM micrograph of one dispersoid on Z[100] of the matrix in 14 YH, and (b) corresponding FFT from the particle shown in (a).

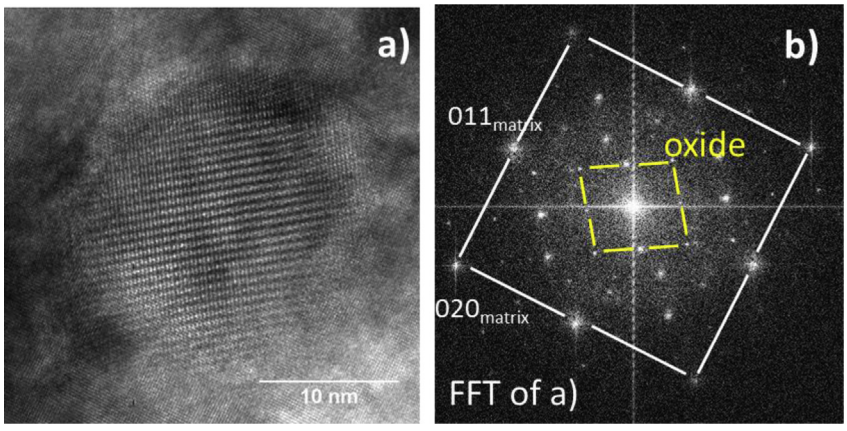

Fig. 10. (a) HR-TEM micrograph of one dispersoid on Z[100] of matrix in 14 YT, and (b) corresponding FFT from the particle shown in (a).

3.4. STEM-EDS

STEM-EDS was used to determine the chemical composition of typical larger (>30 nm) dispersoids in Fig. 11 for alloy 14 YH. The dispersoids are shown by bright contrast in STEM-dark field (DF) and the analyzed area is indicated by the white square. The iron, chromium, yttrium, hafnium and oxygen concentration maps show that the large dispersoids contained yttrium, hafnium and oxygen. The average atomic ratio of metallic elements in the dispersoids was approximately Y:Hf = 5:2. Similarly for alloy 14 YT in Fig. 12, the larger (>30 nm) dispersoids contained yttrium, titanium and oxygen but in atomic ratio of approximately Y:Ti = 1:1.

3.5. APT

The smaller dispersoids in both alloys were too small for reliable analysis by STEM-EDS. However in related work, Zhang et al. [24] had previously studied the identical alloy 14 YT by APT, and

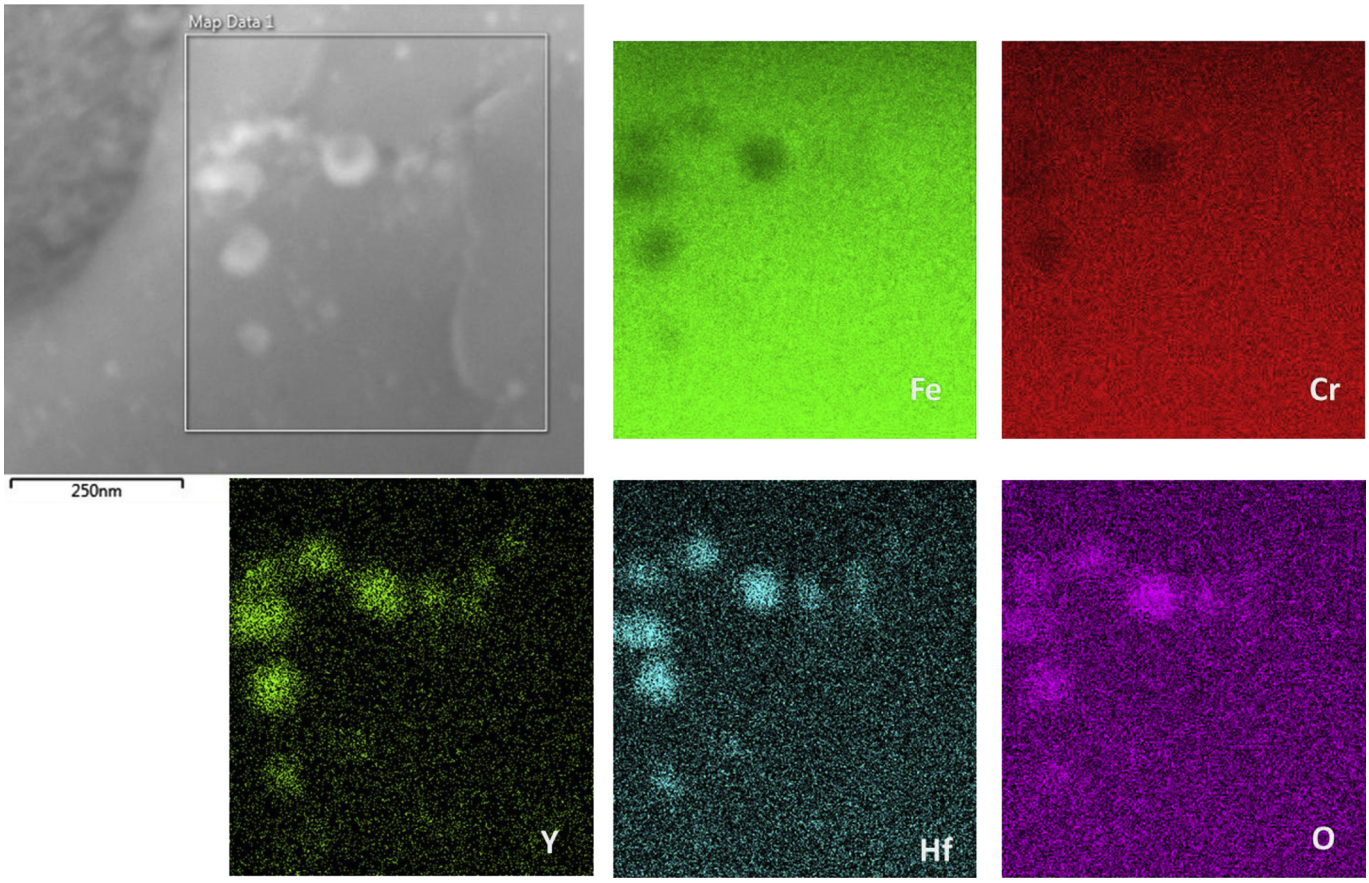

Fig. 11. STEM-EDS elemental maps showing the micro-chemical composition of larger dispersoids in alloy 14 YH. The top left image is the STEM-DF image.

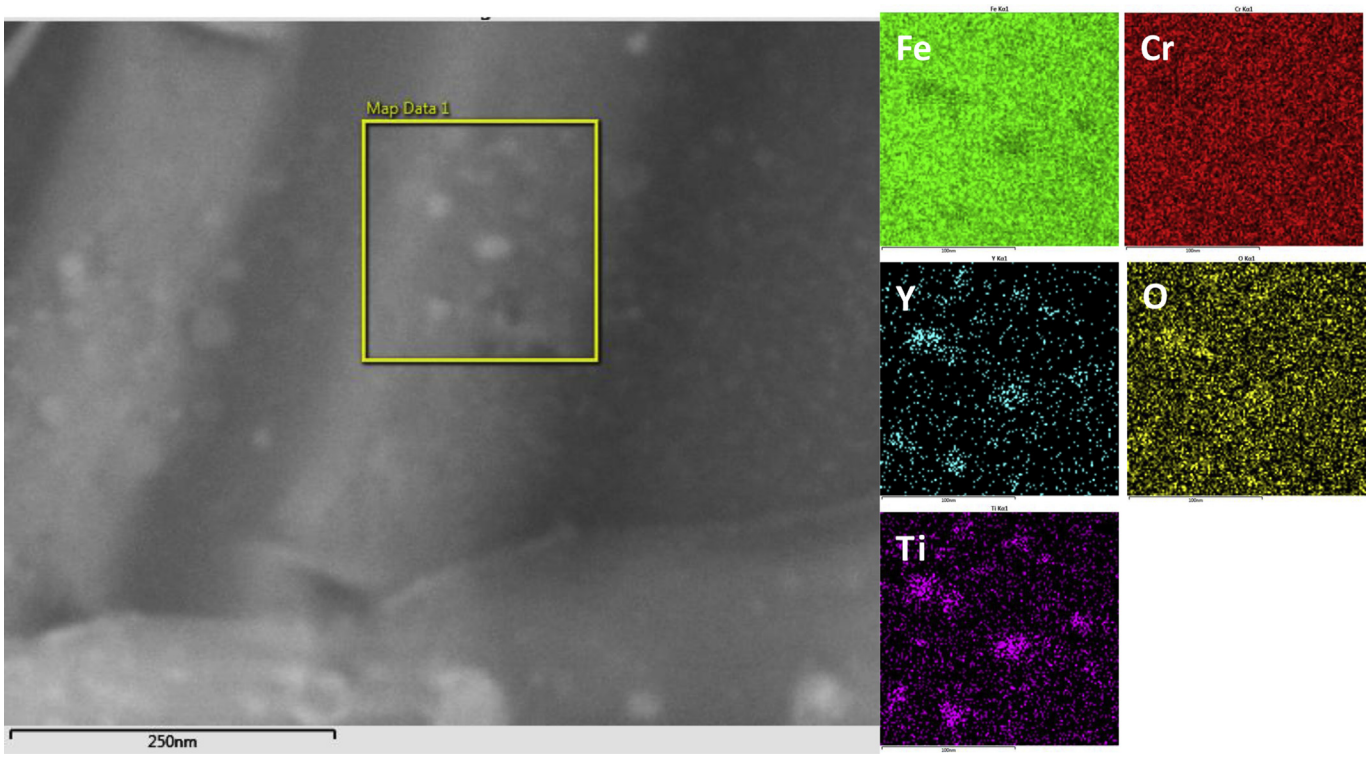

Fig. 12. STEM-EDS elemental maps showing the micro-chemical composition of larger dispersoids in alloy 14 YT. The image on the left is the STEM-DF image.

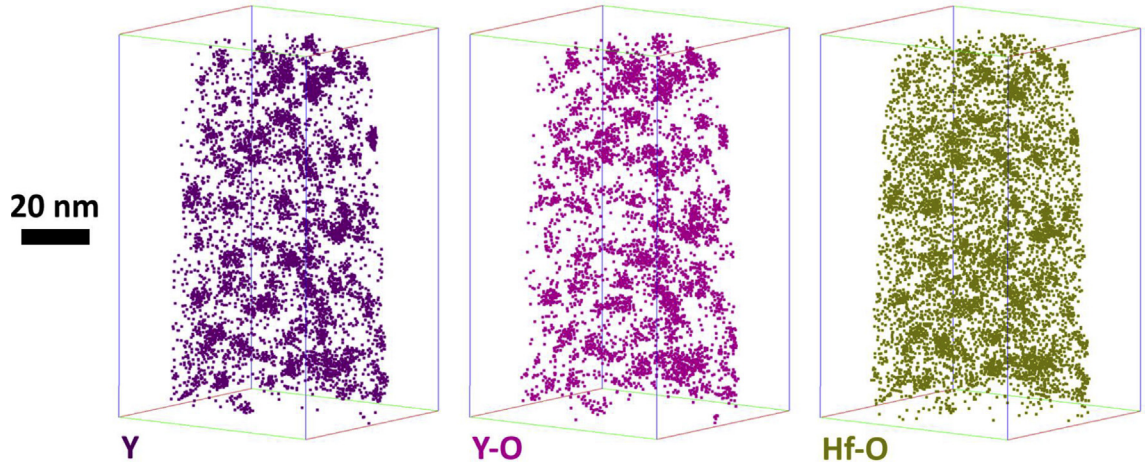

Fig. 13. 3D ion maps reconstructed from APT data for Y, Y-O and Hf-O core-cluster ions in alloy 14 YH.

found that the smaller dispersoids (<5 nm) had a Y:Ti atom ratio close to 1:1, and an estimated dispersoid number density from APT of 2.7 × $10^{23}/m^3$ with an average Guinier diameter of 1.5 ± 0.4 nm.

Following an identical APT approach used in Ref. [24] but now applied to the previously unstudied alloy 14 YH, Fig. 13 shows an APT 3D reconstruction with distinct clustering of Y, Y-O and Hf-O ions. These clusters had a number density of 5 × $10^{23}/m^3$ and a Guinier diameter of 2.9 ± 0.7 nm. The corresponding ion cluster size distribution is shown in Fig. 14. The morphology of the clusters can be approximated from the dimensions of best-fit ellipsoids, as shown in Fig. 15. By APT, the majority of clusters (83%) were spherical, 9% were disc-shaped and 8% were rod-shaped. All the clusters were Y-O rich, and almost all of them (97%) were Y-Hf-O rich. Y, Hf and O concentration in the clusters is shown as a function of cluster size in Fig. 16. The smallest clusters, i.e. <3.5 nm in size, have variable stoichiometry, but those larger than 3.5 nm showed a Y:Hf ratio = 5:2, as displayed in Fig. 17, and in close agreement with the earlier STEM-EDS estimations.

4. Discussion

In ODS steels, yttrium oxide is normally the major dispersoid type [3,33]. Titanium has been used frequently to refine the final dispersoid size distribution [18,24]. In this study, we have investigated the effect of hafnium addition, alongside comparative effects of titanium, as a dispersoid refining additive. While there have been some limited studies on the effect of hafnium on ODS dispersion e.g. in a Co-based ODS alloy [22] and an ODS austenitic stainless steel [20], the results reported here are the first for the more widely studied Fe-14Cr alloy. The choice of 0.22 wt% Hf in the study was purposely to make it comparable to a Fe-Cr-0.25Y_2O_3 (wt. %) alloy previously prepared and characterised [41]. In another separate submitted paper [42], the effectiveness of Hf individually in Fe-14Cr is discussed as well on how Hf promotes a fine distribution of precipitates in the alloy can be compared to the effectiveness of Y.

Both Fe-14Cr pre-alloyed powder and elemental Ti and Hf powders were used as starting materials for mechanical alloying in order to fabricate ODS steels. Due to large surface area and high

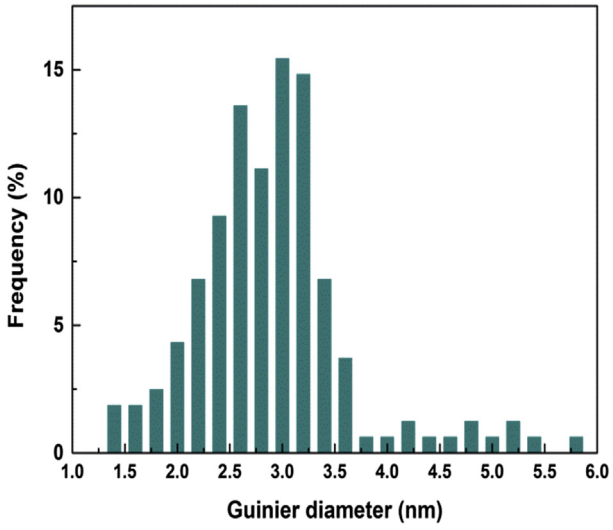

Fig. 14. Size distribution of nano-clusters in alloy 14 YH, obtained from APT data analysis.

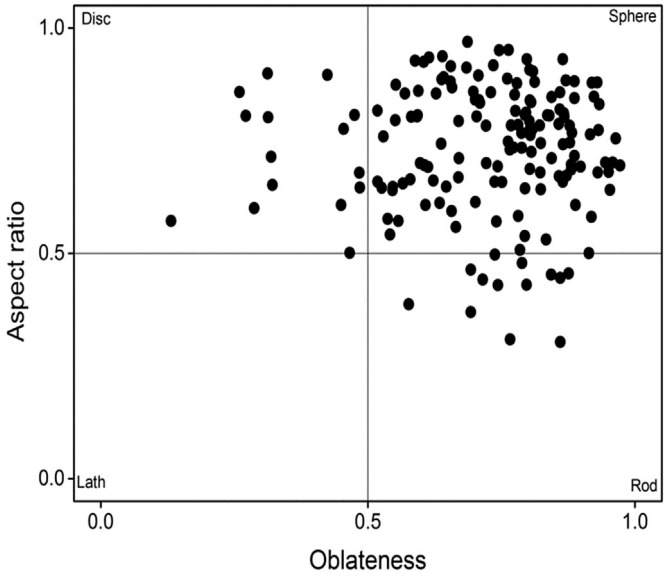

Fig. 15. Cluster morphology distribution in alloy 14 YH, obtained from APT data analysis.

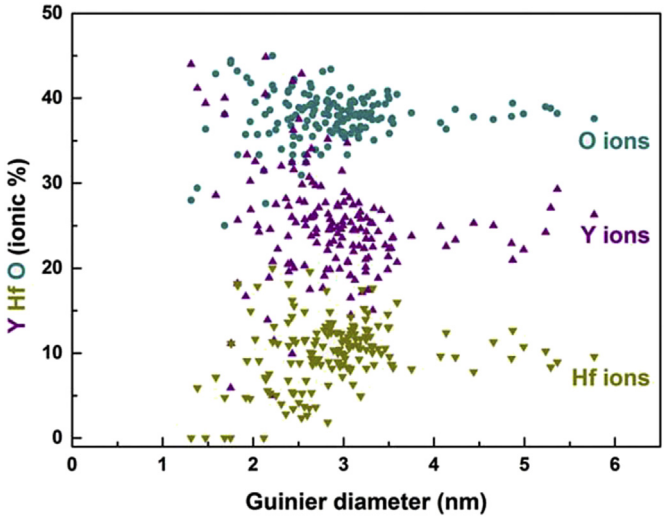

Fig. 16. Y, Hf and O contents as a function of cluster size (Guinier diameter) in alloy 14 YH, obtained from APT data analysis.

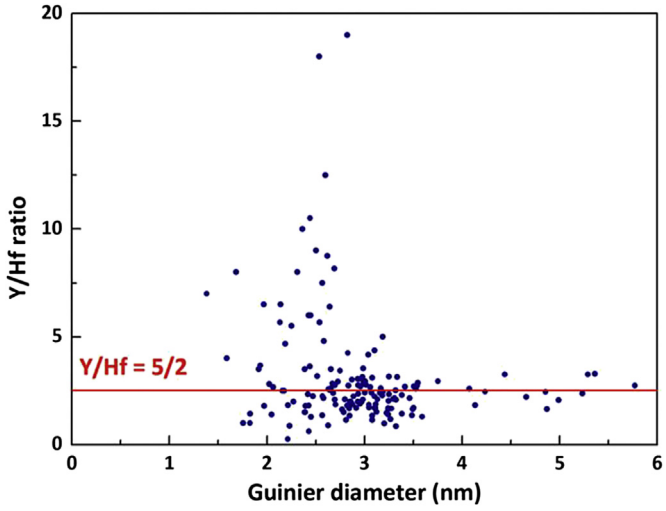

Fig. 17. Y/Hf ratio calculation from APT for the 162 clusters found in the analyzed volume in alloy 14YH.

reactivity of metallic powders, oxygen was inevitably absorbed on the metallic powder particle surface [40]. Both this absorbed oxygen on the metallic powder surfaces and the oxygen contained in the smaller Y_2O_3 powders ensured sufficient oxygen for the formation of Y-Hf oxide and Y-Ti oxide during SPS processing. Overall, the effects of Ti and Hf on the microstructure of the resulting alloys containing Y_2O_3-based dispersoids were rather similar: the dispersoid size distributions in alloys 14 YH and 14 YT in Fig. 7 showed most dispersoids were between 1 and 5 nm in diameter, with a peak size of ~ 2 nm and ~3 nm in the alloys 14 YT and 14 YH, respectively. The dispersoid density in both Ti and Hf containing alloys was ~$10^{23}/m^3$. However, while most dispersoids in 14 YT were of the previously reported $Y_2Ti_2O_7$ type [24], in 14 YH both STEM-EDS data and APT analyses suggested a Y: Hf atomic ratio of 5:2.

Further, the dispersoid compositions for the Hf-containing alloy found here differed from those in previous reports: Oka et al. [20] suggested $Y_2Hf_2O_7$ in an ODS austenitic stainless steel with 0.6 wt % Hf addition; and Zhang et al. [22] suggested that in Co-based ODS alloys two kinds of Y-Hf-O complex were present depending on the Hf concentration: $Y_2Hf_7O_{17}$ ($1Y_2O_3$:$7HfO_2$) at 2.4 wt% Hf and $Y_2Hf_2O_7$ ($1Y_2O_3$:$2HfO_2$) at 1.2 wt% Hf. Neither of these provides a close match to the ratios suggested by both STEM and APT in the present study. There was no strong evidence for Y_2O_3 or HfO_2 i.e. so far as was resolvable using the techniques employed here, Y and Hf always interacted with O together. This difference may arise from the lower Hf concentration used here, which resulted in a further Hf(+Y) containing oxide variant, or subtle differences in the processing history and unresolved differences in the tramp impurity content. Nonetheless, a key finding from the present work is that atom for atom, Hf provides a stronger refining effect on the dispersoid size than Ti.

5. Conclusions

A variety of high resolution characterization techniques have been used to investigate two ODS alloys fabricated by MA followed by SPS consolidation: Fe-14Cr-0.25Y_2O_3-0.22 Hf (14 YH) and Fe-14Cr-0.25Y_2O_3-0.4 Ti (14 YT). Compared with the conventional HIP route for consolidation of ODS alloys [7], where pressures of several hundred MPa and times of several hours are needed, SPS successfully consolidated the alloys at much lower pressure (50 MPa) and shorter time (5 min). The grain structures were similar to those obtained from HIP processing of the same alloys. Yttrium-rich dispersoids were distributed homogeneously in the consolidated alloys, with a number density of ~$10^{23}/m^3$, which is typical for alloys of this type. Hf and Ti additions had similar effects on refining the dispersoid size, even at relatively low Hf concentrations (0.07 at.% Hf vs. 0.46 at.% Ti). Nanoscale chemical data suggested that Hf did not simply substitute for Ti in the dispersoids. While it is likely that both Ti and Hf play a critical role in promoting the nucleation of dispersoids, either directly by forming heterogeneous nucleation sites and extremely fine-scale transition phases, or indirectly by promoting higher dislocation densities, the precise mechanism has yet to be identified. Nonetheless, atom for atom, Hf provided a stronger refining effect on the dispersoid size than Ti.

Acknowledgements

The authors would like to thank the UK Engineering and Physical Science Research Council (EPSRC) for financial support through grant EP/H018921/1 “Materials Fission and Fusion Power”; MG thanks the RCUK Energy Programme for financial support through grant EP/1501045.

References

[1] S. Ukai, Comprehensive nuclear materials, in: Radiation Effects in Structural and Functional Materials for Fission and Fusion Reactors, 4, 2012, pp. 241–271.
[2] T. Muroga, T. Nagasaka, Y. Li, H. Abe, S. Ukai, A. Kimura, T. Okuda, Fusion Eng. Des. 89 (2014) 1717–1722.
[3] S. Ukai, S. Ohtsuka, T. Kaito, H. Sakasegawa, N. Chikata, S. Hayashi, S. Ohnuki, Mat. Sci. Eng. a-Struct. 510–11 (2009) 115–120.
[4] A. Kimura, R. Kasada, N. Iwata, H. Kishimoto, C.H. Zhang, J. Isselin, P. Dou, J.H. Lee, N. Muthukumar, T. Okuda, M. Inoue, S. Ukai, S. Ohnuki, T. Fujisawa, T.F. Abe, J. Nucl. Mater. 417 (2011) 176–179.
[5] H. Oka, M. Watanabe, S. Ohnuki, N. Hashimoto, S. Yamashita, S. Ohtsuka, J. Nucl. Mater. 447 (2014) 248–253.
[6] I. Shibahara, S. Ukai, S. Onose, S. Shikakura, J. Nucl. Mater. 204 (1993) 131–140.
[7] S. Ukai, K. Hatakeyama, S. Mizuta, M. Fujiwara, T. Okuda, J. Nucl. Mater. 307 (2002) 758–762.
[8] P. Unifantowicz, Z. Oksiuta, P. Olier, Y. de Carlan, N. Baluc, Fusion Eng. Des. 86 (2011) 2413–2416.
[9] C. Cayron, E. Rath, I. Chu, S. Launois, J. Nucl. Mater. 335 (2004) 83–102.
[10] M.A. Auger, V. de Castro, T. Leguey, M.A. Monge, A. Munoz, R. Pareja, J. Nucl. Mater. 442 (2013) S142–S147.
[11] M. Tokita, Handbook of Advanced Ceramics: materials, Applications,

Processing, and Properties, second ed., 2013, pp. 1149–1177.
[12] R. Orru, R. Licheri, A.M. Locci, G. Cao, Woodhead Publ. Mater. (2010) 275–303.
[13] B.R. Golla, B. Basu, in: V.K. Sarin, D. Mari, L. Llanes, C.E. Nebel (Eds.), Comprehensive Hard Materials, Elsevier, Amsterdam, 2014, pp. 177–205.
[14] M.A. Auger, V. de Castro, T. Leguey, A. Munoz, R. Pareja, J. Nucl. Mater. 436 (2013) 68–75.
[15] M. Ratti, D. Leuvrey, M.H. Mathon, Y. de Carlan, J. Nucl. Mater. 386–88 (2009) 540–543.
[16] S. Ohtsuka, S. Ukai, M. Fujiwara, T. Kaito, T. Narita, J. Nucl. Mater. 329 (2004) 372–376.
[17] A. Karch, D. Sornin, F. Barcelo, S. Bosonnet, Y. de Carlan, R. Loge, J. Nucl. Mater. 459 (2015) 53–61.
[18] H. Kishimoto, R. Kasada, O. Hashitomi, A. Kimura, J. Nucl. Mater. 386–88 (2009) 533–536.
[19] P. Dou, A. Kimura, R. Kasada, T. Okuda, M. Inoue, S. Ukai, S. Ohnuki, T. Fujisawa, F. Abe, J. Nucl. Mater. 442 (2013) S95–S100.
[20] H. Oka, M. Watanabe, N. Hashimoto, S. Ohnuki, S. Yamashita, S. Ohtsuka, J. Nucl. Mater. 442 (2013) S164–S168.
[21] J.R. Rieken, I.E. Anderson, M.J. Kramer, G.R. Odette, E. Stergar, E. Haney, J. Nucl. Mater. 428 (2012) 65–75.
[22] L. Zhang, S. Ukai, T. Hoshino, S. Hayashi, X.H. Qu, Acta Mater. 57 (2009) 3671–3682.
[23] Q.X. Tang, T. Hoshino, S. Ukai, B. Leng, S. Hayashi, Y.M. Wang, Mater. Trans. 51 (2010) 2019–2024.
[24] H.T. Zhang, Y.N. Huang, H.P. Ning, C.A. Williams, A.J. London, K. Dawson, Z.L. Hong, M.J. Gorley, C.R.M. Grovenor, G.J. Tatlock, S.G. Roberts, M.J. Reece, H.X. Yan, P.S. Grant, J. Nucl. Mater. 464 (2015) 61–68.
[25] Y. Huang, Workshop on TEM Characterization of Irradiation Induced Defects, Argonne National Laboratory, 3rd–5th September 2014.
[26] Z. Jiao, Workshop on TEM Characterization of Irradiation Induced Defects, Argonne National Laboratory, 3rd–5th September 2014.
[27] A. Aitkaliyeva, J.W. Madden, B.D. Miller, J.I. Cole, Micron 67 (2014) 65–73.
[28] A. Prokhodtseva, B. Decamps, R. Schaublin, J. Nucl. Mater. 442 (2013) S786–S789.
[29] P. Miao, G.R. Odette, T. Yamamoto, M. Alinger, D. Hoelzer, D. Gragg, J. Nucl. Mater. 367 (2007) 208–212.
[30] H. Kishimoto, M.J. Alinger, G.R. Odette, T. Yamamoto, J. Nucl. Mater. 329 (2004) 369–371.
[31] P. Dou, A. Kimura, R. Kasada, T. Okuda, M. Inoue, S. Ukai, S. Ohnuki, T. Fujisawa, F. Abe, J. Nucl. Mater. 444 (2014) 441–453.
[32] P. Dou, A. Kimura, T. Okuda, M. Inoue, S. Ukai, S. Ohnuki, T. Fujisawa, F. Abe, J. Nucl. Mater. 417 (2011) 166–170.
[33] M. Klimiankou, R. Lindau, A. Moslang, J. Nucl. Mater. 329 (2004) 347–351.
[34] M.K. Miller, G.D.W. Smith, Atom Probe Microanalysis : Principles and Applications to Materials Problems, Materials Research Society, Pittsburgh, Pa, 1989.
[35] B. Gault, Atom Probe Microscopy, Springer, New York, 2012.
[36] M.K. Miller, Atom Probe Tomography : Analysis at the Atomic Level, Kluwer Academic/Plenum Publishers, New York ; London, 2000.
[37] M.K. Miller, E.A. Kenik, Microsc. Microanal. 10 (2004) 336–341.
[38] R.K.W. Marceau, L.T. Stephenson, C.R. Hutchinson, S.P. Ringer, Ultramicroscopy 111 (2011) 738–742.
[39] H.T. Zhang, M.J. Gorley, K.B. Chong, M.E. Fitzpatrick, S.G. Roberts, P.S. Grant, J. Alloy Compd. 582 (2014) 769–773.
[40] C. Suryanarayana, Prog. Mater. Sci. 46 (2001) 1–184.
[41] I. Hilger, M. Tegel, M.J. Gorley, P.S. Grant, T. Weissgarber, B. Kieback, J. Nucl. Mater. 447 (2014) 242–247.
[42] M. A. Auger, Y. Huang, H. Zhang, C. Jones, Z. Hong, M.P. Moody, S.G. Robert, P. S. Grant. Microstructural and mechanical characterisation of Fe-14Cr-0.22Hf alloy fabricated by spark plasma sintering. Submitt. J. Alloys Compd..